In-Situ Solar Tower Power Plant Optimization by Differentiable Ray Tracing

Abstract

Solar tower power plants deliver climate-neutral electricity and process heat and can play a key role to facilitate the ongoing energy transition. These plants reflect sunlight with thousands of mirrors (heliostats) to a receiver and can generate temperatures over 1000 °C. In practice, a plant must be operated with safety margins as even small surface deformations and heliostat misalignments can locally lead to dangerous temperature peaks. These imperfections are difficult to assess and limit the plant's efficiency, which hinders commercial success in a competitive market. We present a computational technique that predicts the incident power distribution of each heliostat including the inaccuracies based solely on focal spot images that are already acquired in most solar power plants. The method combines differentiable ray tracing with a smooth parametric description of the heliostat and reconstructs flawed mirror surfaces with sub-mm precision. Applied at the solar tower plant in Jülich, our approach outperforms all alternatives in accuracy and reliability. The approach can be integrated into the existing infrastructure and plant control at low cost, leading to increased efficiency of existing and decreased expenses for future power plants and supports establishing a new, green energy technology. For other fields, our approach can be a blueprint. We implement a common simulation technique in the Machine Learning framework PyTorch, leveraging automatic differentiation and GPU computation. By combining gradient-based optimization methods and a tunable parametric heliostat model, we overcome the high data requirements of data-centric methods while at the same time maintaining the flexibility required for modeling a complex real-world system.

Keywords: Solar Tower, Heliostat Field, Differentiable Ray Tracing, Surface Diagnosis, NURBS

Concentrating solar thermal power plants are an essential part of the ongoing energy transition. Their ability to provide direct process heat and store it for days makes it possible to produce carbon-neutral fuels, and generate dispatchable electricity [1–4]. Solar tower power plants stand out here in particular due to their efficiency, competitive levelized cost of energy, and rather low consumption of rare materials compared to photovoltaics [5–7]. Their general setup is displayed in Fig. 1. Thousands of mirrors, the *heliostats*, reflect the sunlight onto one absorbing surface, the *receiver*. The radiation resulting from the superposition of the individual heliostat focal spots can generate thermal power of up to 150 MW on temperature levels of more than 1000 °C. However, thermal stress and heat peaks significantly reduce the longevity of the power plant's components, forcing operators to run smaller temperatures and thus lower efficiencies. To reach these temperatures safely, the heliostats must hit the receiver precisely at an intended location and with a specific power distribution. However, due to cost constraints affecting especially the material and component quality of the heliostats, the required accuracy is difficult to achieve. The two most influential heliostat deficiencies are misalignments and focal spot deformations.

Heliostat misalignment can be corrected for by the so-called heliostat calibration, which is regularly carried out at solar towers. The most common method is the *camera-target* method [8]. The focal spot of each heliostat is moved individually from the receiver to a white target, which is usually located below the receiver (see Fig. 1). Using geometric knowledge and a photograph of the focal spot, the true heliostat alignment can be calculated. This process is fully automated

Fig. 1: Image of the two solar towers in Jülich. The heliostats, shown from behind, are focusing sunlight on the receiver surface of the left tower. Located below the receiver is the calibration target. The inset shows a focal spot image as it is taken during calibration.

and integrated in most solar power plants. In principle, the deviation of the mirror surface from an ideal geometry can be laboriously inferred by fringe pattern deflectometry [9–11]. In this method, a fringe pattern is projected onto the calibration target and its reflection on the heliostat is analyzed using camera images. The shape of the heliostat (represented by its normal vectors) can be deduced from the curvature of the stripes. While this method delivers very accurate results, it remains challenging for industrial-scale application because environmental variance, measurements at night, high distances, dust, and dew prevent any automated operation.

We here present a novel machine learning solution that allows for inferring all faulty heliostat characteristics within the existing heliostat calibration infrastructure. Our technique ties in with common ray tracing approaches, but extends them by a differentiable formulation [12–19]. This allows us to define a comprehensive heliostat model which can be inferred using gradient-based optimization procedures. These heliostats can be integrated into a digital twin of the solar power plant and be a key ingredient for optimizing plant operations. Using this method, we can predict heliostat-specific irradiance profiles with unprecedented accuracy. It also reconstructs the heliostat's surface profile with a precision similar to that of standard deflectometry, yet only requires calibration images taken on a day-to-day basis. To evaluate our method, we conducted an experimental proof of concept at the research power plant in Jülich. In complementary simulations, we show that our approach is applicable for the whole heliostat array. The approach consistently improves the annual irradiance forecast, allowing for higher plant efficiencies at minimal cost. This contribution is a crucial step towards the development of concentrating solar power plants into a cost-efficient, environmentally friendly, alternative source of process heat and dispatchable energy.

Differentiable Ray Tracing for Solar Towers

We here outline a physical model of solar towers as in Fig. 1 and its differentiable implementation. The calibration target's surface is matte and well approximated by a Lambertian surface, where the reflected light is proportional to the surface irradiance, independent of the observer's viewpoint. The irradiance at position $\vec{x}$ on the calibration target can be obtained by integrating the radiance L over all incoming directions $\vec{\omega}$, multiplied by the cosine of the incident angle θ. Neglecting ambient lighting, the incident irradiance can be constructed by finding the intersection $\vec{r}$ of the incident direction with the heliostat, and – if within the heliostat surface – constructing the reflected direction ω_r by evaluating the local heliostat normal and evaluating the solar radiance $L_\odot$ in the reflected direction. This reads as

$$E\left(\vec{x}\right) = \int\limits_{\Omega} L_\odot\left(\vec{\omega}_r\left(\vec{\omega}, \vec{r}\right)\right) \cos\theta \, d\vec{\omega}.$$

This can include taking into account a model of the deviation of the surface from ideally flat, which we express by a reflection function $\vec{\omega}_r$ that depends on the heliostat surface point $\vec{r}$. In this formulation, most ray directions will not contribute to the irradiance of a point on the target surface, as the solar disk is small. Alternatively, the integral can be cast as an integral over incident directions. Then, by using *importance sampling*[20], the rays' directions can be sampled with a probability proportional to the respective solar radiance. This minimizes the required number of rays. For each ray, the intersection with the target surface $\vec{x}$ is evaluated. Up to this point, the presented ray tracing scheme is common in the domain [12–19]. A modified last step, however, is crucial to ensure differentiability of the approach. Typically, the discrete rays are binned by their intersection point $\vec{x}$ on the receiver with a hard binning scheme. There, the incident ray power is accumulated in the nearest point in a grid on the target. In our formulation, we employ a soft binning function w, that smoothly distributes the power of ray $\vec{k}$ cast from heliostat point $\vec{l}$ to more than one grid point on the target. Hence, for each grid point $\vec{x}_{ij}$, the irradiance is a weighted sum over all rays cast from heliostat surface point $\vec{r}_l$ in direction $\vec{t}_{\vec{k}}$,

$$E\left(\vec{x}_{ij}\right) \propto \sum_{\substack{\text{ray } \vec{k},\\ \text{position } \vec{l}}} \underbrace{w\left(\vec{x}_{ij}, \vec{x}\left(\vec{r}_l, \vec{t}_{\vec{k}}\right)\right)}_{w_{ijkl}} \cos\theta. \tag{1}$$

Our employed differentiable binning scheme is inspired by a technique employed for coupling the Lattice Boltzmann equation with molecular dynamics simulations and distributes each incoming ray linearly to the 4 closest, discrete points on the receiver's surface [21].

In the description above, we have assumed that for each position of the heliostat, it is possible to construct the reflection of a ray, which requires a differentiable surface model. Furthermore, it is physically justified that heliostat surfaces are smooth. We therefore choose to model the heliostat surface in terms of *Non-Uniform Rational B-Spline* (NURBS) surfaces [22]. This formulation automatically ensures a smooth, differentiable surface model and gives maximum flexibility to include deformations with a variable degree of detail.

In the optimization procedure, we define the optimization objective as a distance between an observed image and an image reconstructed by the ray tracing described above, which we dub the *loss*. Subject to optimization are the control point positions of the NURBS. As the formulation is differentiable, the loss can be minimized with gradient-based optimization algorithms. In this formulation, it is possible to include regularization terms. For optimization problems, such terms can reduce the complexity of possible solutions and mitigate the ill-posedness of the problem. In the case of the heliostat, we prefer solutions that minimize the deviations from an ideally flat heliostat surface. This is realized as a term that penalizes deviations of the NURBS control points from ideal positions. The corresponding regularization factors can be tuned to the details of the optimization problem.

The code is implemented in the Machine Learning framework PyTorch [23].

Irradiance Prediction at the Solar Tower in Jülich

In this section, we benchmark our approach at the solar tower in Jülich. This research power plant can generate rated electrical power of up to 1.5 MW by using over 2000 heliostats at a distance between 25 m–250 m. Each heliostat has four individual facets, which are *canted*, i.e. tilted to a joint focus, and use an astigmatically corrected target alignment [24].The canting leads to overlapping focal spots of the individual facets. Therefore, the minimum of the optimization can not be expected to be unique – this optimization problem can be underdetermined. For the validation procedure, we selected a heliostat in the first row of the field. In end of October (2021-10-21), we measured the heliostat's surface using deflectometry. On a later day with clear sky conditions (2022-03-04), we executed the regular calibration procedure for the same heliostat at two times of the day. The images provided by these calibrations are used for training. After that, the next regular calibration was due in approximately 8 months. Two images acquired during those calibrations are used as the test data set.

Fig. 2 shows the recorded images in the leftmost column (*Measurement*). The average value of the pixel intensity was subtracted from the recorded raw images (compare Fig. 1) and the

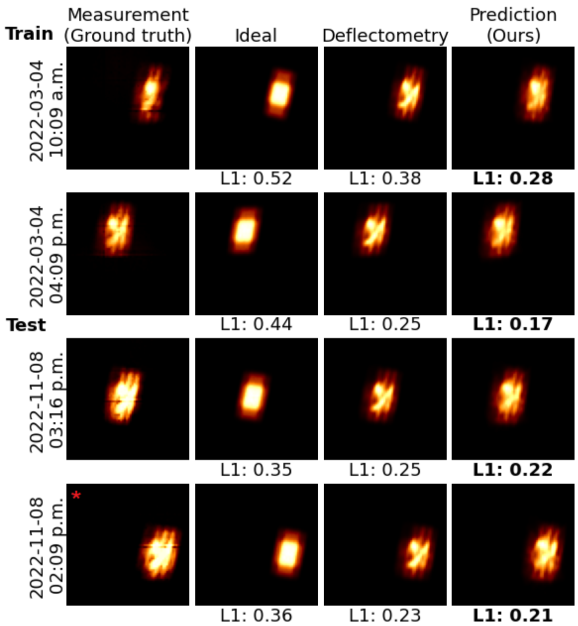

Fig. 2: Comparison of the irradiance profiles of a *Measurement* photograph and ray tracing with a flat surface (*Ideal*), a measured surface (*Deflectometry*), and the result of our optimization procedure (*Prediction*). The deviation between the measurement and each generated image is quantified using the L1 distance. The image marked with a red star was previously shown in Fig. 1.

pixel values were normalized. The column *Ideal* displays the irradiance inferred by a ray tracing method that assumes a flat heliostat. This column also represents the state-of-the-art. In the column *Deflectometry*, we report ray tracing results that use the surface obtained from the deflectometry measurement. The right-most column are our data-driven optimization results. As the non-data-driven approaches have no information about misalignments, our ray tracing pipeline was used to correct the heliostat's alignment and rotation in all results for better comparability. For evaluation, we use the mean absolute error, and report it as *L1*. The images are normalized to the incoming intensity and scaled by the calibration target plane. This way, the loss is independent from resolution and size.

It is evident that using the deflectometrically measured surface in our ray tracer delivers excellent results. As the literature suggests, we can confirm that these surfaces can be used for high-quality irradiance prediction. However, our method performs comparably and does not need additional measurements requiring conditions which are difficult to meet.

In simulation, we can furthermore study more characteristics of our method by performing training on simulated data with the measured surface. The results are summarized in Fig. 3. The left panel (a) shows how the differentiable ray tracing approach performs on the shortest and the longest day, as well as at equinox, when the deformations are especially noticable. If trained on 16 images, the prediction's error metric L1 can be reduced by almost an order of magnitude compared to simulations based on ideally flat surfaces. Depending on the distance, the characteristics of the spot change considerably. The focal spot softens and becomes larger, which can be seen in the upper right panel (b).

In the graph in panel (c), we study the performance of the approach quantitatively by varying both the heliostat position and the number of available training images. The measured heliostat is in the first row of the field (25 m north of the solar tower). In the simulations, we vary its position, and accordingly canting angle as well as focal length. We also observe the L1 reduction by one order of magnitude down to a training set size of only 4 images. Our method is even able to reconstruct the focal spots with high precision using only 2 training images. The test loss was calculated on a disjoint data set of five images which were not used during training.

Heliostat Surface Reconstruction

Our simulation method is based on physical principles, and we therefore expect a reconstruction of a physically meaningful surface. However due to the overlap of the focal spots of the canted facets and the blur increasing with distance, it is not clear that the optimization problem exhibits a unique, physically meaningful minimum. Our experiments indicate that – under favorable conditions – the real surface can be obtained. The surface already used in the previous chapters is shown in Fig. 4 by its deviation from the ideal surface. In the preparation process, we manually applied a geometric modification by tightening the

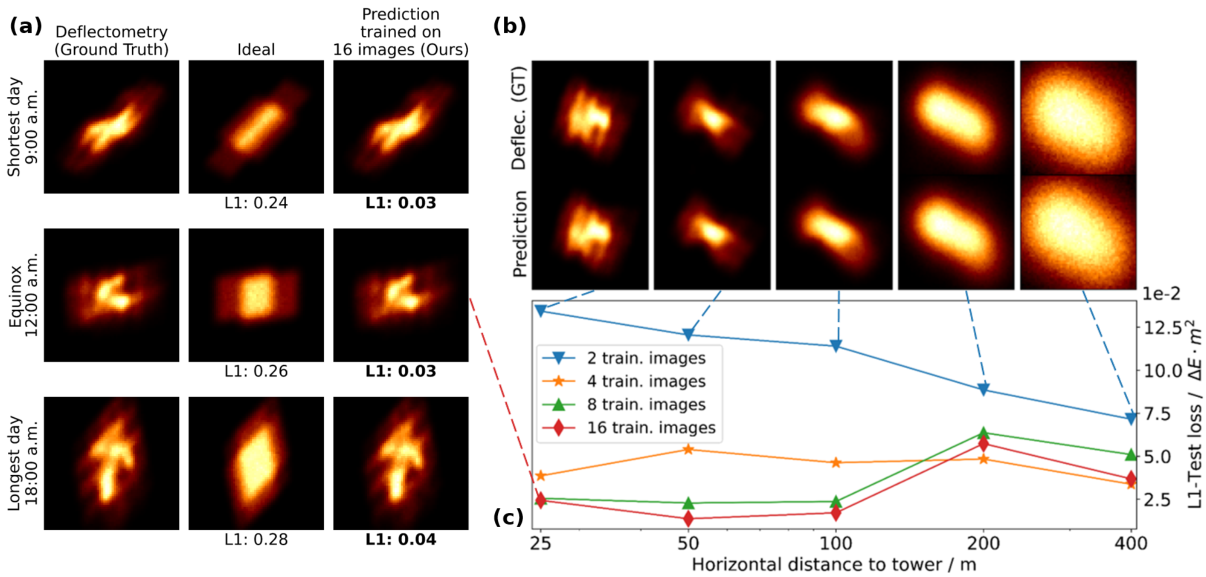

Fig. 3: (a) Comparison of the irradiance profile on three days of the year. We compare the simulation with the measured surface, a simulation with an ideal surface and the result of our approach trained on 16 images. Our method predicts the complex structures accurately. (b) Simulated and inferred irradiance profiles at different distances between heliostat and target. (c) Quantitative assessment of prediction quality for varying distances and number of training images.

adjustment screws at the center of all four facets to obtain a characteristic "bump" deformation of approximately 2 mm, which is in the range of heliostat surface defects. This way, we made sure that already at first glance, a qualitative judgment of a surface reconstruction is possible. Below the shown measured surface are two columns with reconstructions created by our method. Reconstructions in the left column are obtained by varying the number of training data, while for the right column, the distance of the heliostat to the tower was varied. The results are summarized quantitatively in the graph below. The surface can be reconstructed in more than 100 m distance to the tower. Beyond that, the reconstruction quickly degrades. Interestingly, the quality of the irradiance reconstruction as displayed in Fig. 3 is barely affected.

The surface reconstruction is based on simulated data supported by a deflectometric measurement of the surface. With the available imagery from the calibrations, a qualitative surface reconstruction of the surface was not possible (not shown). By gathering more data and careful tuning of the optimization procedure, we expect this to be possible. However, our previous findings indicate that surface reconstruction is not required for accurate irradiance predictions. Preliminary experiments indicate that difficulties in reconstruction are largely caused by the canting and related ambiguity. By hypothetically positioning the calibration target at a distance outside of the focal plane or employing heliostats without canting, the surface reconstruction works significantly better and requires smaller training sets.

Conclusion & Outlook

In this article, we show that differential rendering is an approach that is very well suited for the in-situ application at solar towers. By using images from the fully automated heliostat calibration, which is already implemented in most solar power plants, our approach is capable of predicting the irradiance with unprecedented accuracy. Our approach outperforms state-of-the-art ray tracing approaches in day-to-day use by far. The results on experimental data from the plant show that the method yields high-quality irradiance predictions, and our in-silico experiments indicate that these findings can be generalized to the entire

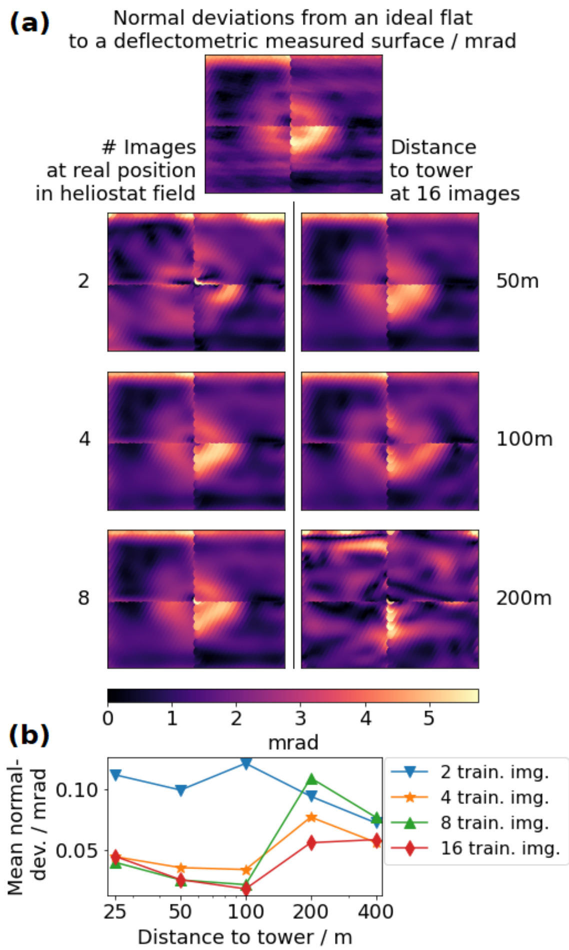

Fig. 4: (a) Surface reconstructions from focal spot images depending on data set (left column) and on the distance to the tower (right column). The surfaces are represented by the deviation in mrad of their normals from the ideal surface. (b) Quantitative assessment of the reconstruction quality. For distances of 100 m or less, the surface can be reconstructed qualitatively with at least four training images.

heliostat field.
Furthermore, it is the very first method to derive information from heliostat focal spots to reconstruct the corresponding surface deformations. Due to the computational efficiency and small data footprint, it can be implemented with relatively low cost. Existing calibration infrastructure can be used, and only software adjustments are required.
The methodological principles have notable strengths: without restrictions, it is a physically motivated model, which on the one hand has enough parameters to represent reality completely, and on the other hand offers a flexible regularization of surfaces to deliver excellent irradiance predictions, even in underdetermined regimes. For industrial-scale application, the surface model and the regularization can be optimized, taking into account the availability and quality of data, as well as heliostat characteristics. This is exemplified in the Methods section (p. 6). A careful choice of a different calibration target position can mitigate the ambiguity and improve the surface reconstruction.
Ray tracing has occupied a central place in solar tower research even before this study. Through the very first realization of differentiability, it is now possible to employ ray tracing at the solar tower in a data-driven way. Its applicability combined with high-quality results will ensure that it takes on an even more important, key role. Differentiable ray tracing will be a decisive step to higher power plant efficiencies, by optimizing not only the irradiance prediction, but also almost all material and object properties in the solar field, like the heliostat's alignment. Our digital twin is a key ingredient for an efficient, autonomous and intelligent solar power plant.

Methods

Differentiable Simulation

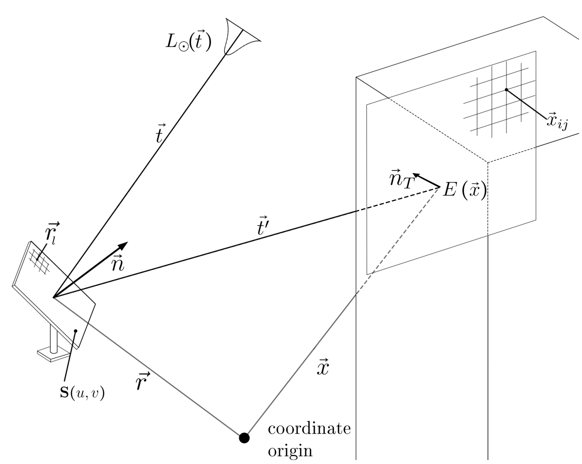

Fig. 5: Sketch of the used coordinate system.

Here, we provide the key equations that form the proposed model. Our starting point is the radiance, the quantity that describes the radiation field in terms of power per area and solid angle (W/m^{2}sr). It is given by L, which depends on the position $\vec{x}$ and the direction $\vec{t}$. In non-absorbing media, it is constant along any line, here parameterized with the scalar λ.

$$L\left(\vec{x}, \vec{t}\right) = L\left(\vec{x} + \lambda \vec{t}, \vec{t}\right) \qquad \forall \lambda.$$

The radiance field $L_\odot$, created by the sun visible in direction $\vec{t}_\odot$, can be well approximated by a Gaussian distribution:

$$L_\odot \propto e^{-\left(\frac{\arccos \vec{t}\cdot\vec{t}_\odot}{\theta_\odot}\right)^2},$$

with an aperture angle of $\theta_\odot = 0.00025°$. In order to obtain the irradiance $E\left(\vec{x}\right)$, the power per surface area at position $\vec{x}$ on a surface, integration over the solid angle is required. This includes the cosine factor that is well known from e.g. the rendering equation [25, 26]. This reads as

$$E\left(\vec{x}\right) = \int_\Omega L\left(\vec{x}, \vec{t'}\right) \ \vec{n}_T \cdot \vec{t} \quad d\Omega,$$

with $\vec{n}_T$ the normal vector of the calibration target and $\vec{t'}$ the unit vector indicating the direction that is evaluated. For a given point on the target, this integral can be evaluated in the following way: for each direction on the unit hemisphere, the corresponding intersection $\vec{r}$ with the heliostat is calculated, and the solar radiance is evaluated in the direction that is obtained from evaluating the reflection condition for the heliostat surface. The drawback is that, depending on the system's geometry, a large fraction of the evaluated direction vectors will not intersect with the heliostat surface or will lead to directions where the solar radiance is negligible.

The integral can be transformed into a surface integral over the heliostat surface A. This reads as

$$E\left(\vec{x}\right) = 4\pi \int_A L_\odot\left(\vec{r}, \vec{t}\right) \ \vec{n}_T \cdot \vec{t'} \frac{\vec{n}_H \cdot \vec{t'}}{\left\|\vec{x} - \vec{r}\right\|^2} \quad \mathrm{d}A,$$

where $\vec{t}$ is the unit vector pointing from the target point $\vec{x}$ to the heliostat point $\vec{r}$. The vector $\vec{t'}$ is the direction that is obtained as the reflection of $\vec{t}$. With a curved heliostat, this direction can be obtained by evaluating the heliostat normal $\vec{n}_H = \left[n_1, n_2, n_3\right]^t$ at position $\vec{r}$ and constructing the reflection matrix $M\left(\vec{r}\right)$ as

$$M\left(\vec{r}\right) = \begin{pmatrix} 1-2n_1^2 & -2n_1n_2 & -2n_1n_3 \\ -2n_1n_2 & 1-2n_2^2 & -2n_2n_3 \\ -2n_1n_3 & -2n_2n_3 & 1-2n_3^2 \end{pmatrix}.$$

Then, the reflected direction can be obtained as $\vec{t} = M \cdot \vec{t'}$. By introducing the Dirac δ function, we can formally introduce an integration over all directions $\vec{t'}$. We obtain

$$E\left(\vec{x}\right) = c \int_A \int_{\Omega'} L\left(\vec{r}, \vec{t'}\right) \delta\left(\vec{x} - \vec{x}_{\vec{t}}\right) \mathrm{d}\Omega' \mathrm{d}A,$$

where $\vec{x}_{\vec{t}}$ is the intersection of a ray incident from the sun from direction $\vec{t'}$ with the target plane after reflection. Due to the large distance of the heliostat to the target and the small change of normal of the heliostat, the other terms can be considered constant and absorbed in a prefactor c. What seems like a mathematical trick at first has a simple physical interpretation. Before, we traced rays under all incident angles to the sun. Now, for all positions $\vec{r}$ on the heliostat surface, we cast rays in all possible directions $\vec{t'}$ and evaluate each ray's contribution to the surface irradiance. In practice, we evaluate this integral by sampling rays from a directional distribution proportional to $L_\odot$ and discretizing the heliostat with a rectangular grid. We also discretize the target surface and interpret the δ function as a set of weights that are nonzero only on grid points in the vicinity of $\vec{x}_{\vec{t}}$. This weight idea illustrated in Fig. 6. If $\vec{x}_{ij}$ is the grid point to the lower left of the intersection point $\vec{x}_{\vec{t}}$, the ray is distributed to the four nearest neighbors with

$$\begin{aligned} w_{i,j} &= \left(1 - \Delta_x\right)\left(1 - \Delta_y\right) \\ w_{i+1,j} &= \Delta_x \left(1 - \Delta_y\right) \\ w_{i,j+1} &= \left(1 - \Delta_x\right)\Delta_y \\ w_{i+1,j+1} &= \Delta_x \Delta_y \end{aligned}$$

where Δ_x and Δ_y measure the distance of $\vec{x}_{\vec{t}}$ to $\vec{x}_{ij}$ in units of the grid constant. With this formulation, each ray carries an irradiance contribution that is differentiable with respect to the ray's direction. By introducing these weights, we arrive at Eq. 1.

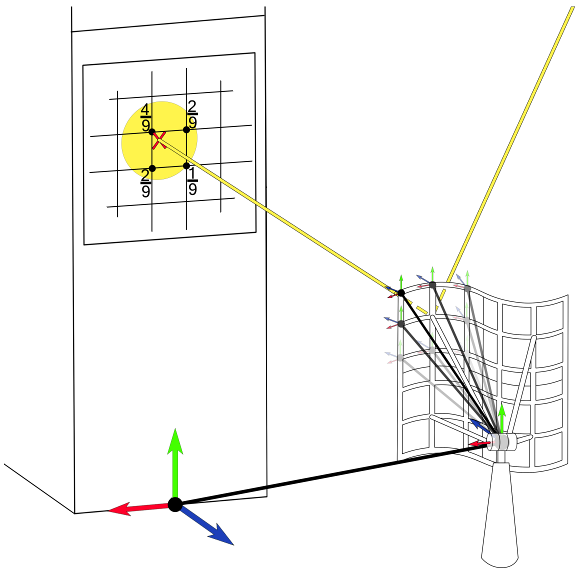

Fig. 6: Schematic drawing of the ray tracing process, including the binning function. The calculation starts at a heliostat lattice point. There, the incoming ray is reflected and traced to the target. Then, the incoming ray's intensity is linearly distributed to the $N = 4$ nearest lattice points. It also shows how the different coordinate systems (tower → heliostat → facet point) are linked together. A rotation of the heliostat automatically influences all downstream coordinate systems.

Heliostat Model

In this section, we will discuss our model of the heliostat. In the setup of the solar tower in Jülich, each heliostat has two angular degrees of freedom, which are set up such that a hypothetical line connecting the sun and the heliostat exactly is reflected into the position on the receiver or the calibration target, where the light should be reflected. Furthermore, each heliostat consists of four facets, i.e. nearly planar square surfaces. These facets are *canted*, i.e. they are inclined such that the areas to which each facets reflects the sunlight overlap. In this work, we assume that these parameters, i.e. heliostat orientation and canting angles are well known. In future works, we can treat these degrees of freedom as subject to an optimization procedure. For example, in preliminary work it was shown, that this approach is able to replace the standard calibration procedure [27] and optimize field design [28]. In the mathematical model, the heliostat surface appears on the one hand as the spatial region where reflection of rays happens. On the other hand, its surface, or more precisely, the local normal vector $\vec{n}\left(\vec{r}\right)$, is the decisive element for the direction in which rays are reflected. As of the large distances between heliostat and target, the resulting radiance $E\left(\vec{x}\right)$ is highly sensitive to changes of this vector. We model each facet as a nearly planar surface. Each facet is placed in the heliostat coordinate system, which is aligned such that given a solar position, the line connecting the sun and the heliostat is reflected exactly into the target. Due to the mechanical stiffness of the reflective surface, it is justified to assume only a limited curvature of the heliostat facets. As of this smoothness property, we choose to model the deviation of the facet from an ideally flat surface as a Non-Uniform Rational B-Spline (NURBS), a class of functions that is very well suited for representing smooth surfaces. A NURBS surface is composed of different *B-spline* functions and their weighted control points. Each point on the NURBS surface is thereby uniquely defined by a set of points P (control points), W (weights), U, and V (knot vectors), often expressed as [29]:

$$S = f\left(P, W, U, V\right). \tag{2}$$

A surface is parametrized by the variables u and v, where $0 \leq u, v \leq 1$. Evaluated at an point (u, v), the corresponding surface point in 3d-Space is defined as follows (also compare Fig. 5):

$$S\left(u, v\right) = \frac{\sum_{i=0}^{n} \sum_{j=0}^{m} N_i^p\left(u\right) N_j^q\left(v\right) W_{ij} P_{ij}}{\sum_{i=0}^{n} \sum_{j=0}^{m} N_i^p\left(u\right) N_j^q\left(v\right) W_{ij}}. \tag{3}$$

Here, we assume a regular square grid of control points indexed by i and j. The polynomials N_i^p

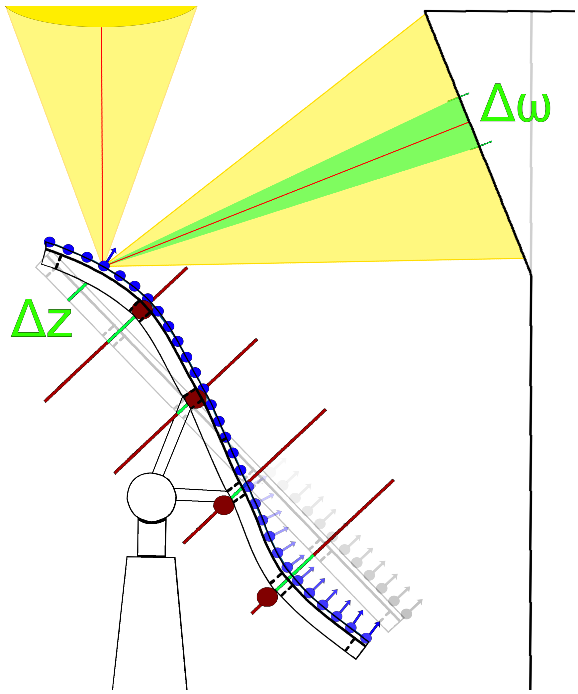

Fig. 7: Schematic drawing of a heliostat NURBS surface. The control points P (red dots) are shifted in the z direction (green section on red line) away from the ideal surface (grey). The deformation affects a specified amount of neighboring discrete points controlled by the spline degree modulating the normal vectors (blue). One discrete point is moved by Δz, which is influencing the ray direction by Δw. The information about the infinitesimal change Δw can be traced back via automatic differentiation to the change of the NURBS control points.

with are defined recursively:

$$\begin{aligned} N_i^p(u) = & \frac{u - u_i}{u_{i+p} - u_i} N_i^{p-1}(u) \\ & + \frac{u_{i+p+1} - u}{u_{i+p+1} - u_{i+1}} N_{i+1}^{p-1}(u) \\ N_i^0(u) = & \begin{cases} 1 & \text{if } u_i \leq u < u_{i+1} \\ 0 & \text{otherwise.} \end{cases} \end{aligned} \tag{4}$$

Here N_i, N_j represent the B-spline basis functions in the representation of *Curry and Schoenberg* [30]. The degree of the polynomial can be chosen freely. The NURBS degree determines how many nodes are affected by another node's change. The smaller the degree, the more local the modification can be. For the mirror facet, a higher degree therefore can be interpreted as a regularizing effect that counteracts high local curvature. Therefore, higher NURBS degrees have proven helpful for small numbers of observed images.

Tangential vectors of the NURBS surfaces can be obtained by taking the derivates with respect to u and v and the local normal vectors are obtained by taking the cross product.

Within the ray tracing environment, the initial NURBS surface is chosen so that N control points are evenly distributed over the heliostat's surface. Schematically, this is visualized in Fig. 7 by the red dots. For the ray tracing process, any number of points M is sampled along the surface (blue points), where $N \ll M$. The position of these M points can be identical with e.g. those of the measured deflectometry surface data. At these points, rays are reflected and transmitted to the receiver/cal. target. The resulting focal spot can be compared with a measured focal spot and the heliostat surface adjusted accordingly. The NURBS surface model has a number of potential advantages that we did not make full use of. For example, we found it sufficient to set all weights to unity, which effectively renders our surfaces conventional B-splines. Furthermore, the in-plane positions of the control points were held fixed and we did not make any use of the relative ease of adding control points on demand, even though code preparations have already been performed.
The results shown in the article were carried out with different NURBS configurations. We found that with our heliostat type. 7×7 NURBS per facet with a spline degree of 3 yield an optimal reconstruction of the surface. In contrast, 11×11 NURBS with a spline degree of 2 are particularly well suited for flux density prediction This can be seen in Fig 8. We explain this difference by the underdetermined nature of the problem. The reduced number of 7×7 NURBS and the higher interlocking allows us to reconstruct the surface features that can still be unambiguously assigned. However, details are lost that affect the quality of the predicted focal spot. 11×11 NURBS provide more degrees of freedom and the optimization procedure converges to physically not justified minima, which however lead to a very accurate focal spot prediction.

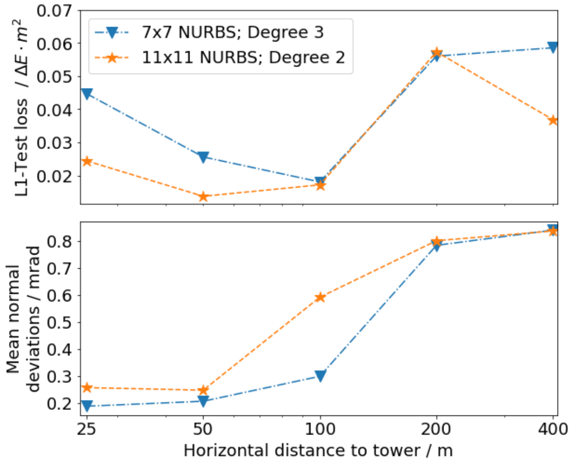

Fig. 8: Predictions of the irradiance and reconstruction of the heliostat's surface with regard to the amount of NURBS parameters and the distance to the tower.

Competing Interests

The authors declare no competing interests.

References

[1] Schäppi, R., Rutz, D., Dähler, F., Muroyama, A., Haueter, P., Lilliestam, J., Patt, A., Furler, P., Steinfeld, A.: Drop-in fuels from sunlight and air. Nature **601**(7891), 63–68 (2022)

[2] Pregger, T., Graf, D., Krewitt, W., Sattler, C., Roeb, M., Möller, S.: Prospects of solar thermal hydrogen production processes. International journal of hydrogen energy **34**(10), 4256–4267 (2009)

[3] Lovins, A.: Decarbonizing our toughest sectors-profitably. MIT Sloan Management Review **63**(1), 46–55 (2021)

[4] Zhongming, Z., Linong, L., Wangqiang, Z., Wei, L., et al.: Solar power for sustainable pasta (2020)

[5] IRENA, I.R.E.A.: Renewable Energy and Jobs – Annual Review 2020. International Renewable Energy Agency (IRENA), Abu Dhabi (2019). https://books.google.de/books?id=0Z8JEAAAQBAJ

[6] Arvizu, D., Balaya, P., Cabeza, L., Hollands, T., Waldau, J., Kondo, M., Konseibo, C., Meleshko, V., Stein, W., Tamaura, Y., et al.: Direct solar energy (2011)

[7] Schöniger, F., Thonig, R., Resch, G., Lilliestam, J.: Making the sun shine at night: comparing the cost of dispatchable concentrating solar power and photovoltaics with storage. Energy Sources, Part B: Economics, Planning, and Policy, 1–20 (2021)

[8] Stone, K.W.: Automatic heliostat track alignment method. Google Patents. US Patent 4,564,275 (1986)

[9] Ulmer, S., März, T., Prahl, C., Reinalter, W., Belhomme, B.: Automated high resolution measurement of heliostat slope errors. Solar Energy **85**(4), 681–687 (2011)

[10] Rapp, H.H.: Reconstruction of Specular Reflective Surfaces Using Auto-calibrating Deflectometry vol. 23. KIT Scientific Publishing, Karlsruhe (2013)

[11] März, T., Prahl, C., Ulmer, S., Wilbert, S., Weber, C.: Validation of two optical measurement methods for the qualification of the shape accuracy of mirror panels for concentrating solar systems. Journal of Solar Energy Engineering **133**(3) (2011)

[12] Belhomme, B., Pitz-Paal, R., Schwarzbözl, P., Ulmer, S.: A new fast ray tracing tool for high-precision simulation of heliostat fields. Journal of Solar Energy Engineering **131**(3) (2009)

[13] Wendelin, T., Dobos, A., Lewandowski, A.: Soltrace: a ray-tracing code for complex solar optical systems. Technical report (2013)

[14] Yu, Q., Wang, Z., Xu, E., Zhang, H., Lu, Z., Wei, X.: Modeling and simulation of 1mwe solar tower plant's solar flux distribution on the central cavity receiver. Simulation Modelling Practice and Theory **29**, 123–136 (2012). https://doi.org/10.1016/j.simpat.2012.07.011

[15] Cardoso, A., Marakkos, C., Schoettl, T.

Peter, Les: New functionalities for the tonatiuh ray-tracing software. In: AIP Conference Proceedings, vol. 2033, p. 210010 (2018). AIP Publishing LLC

[16] Cardona, G., Pujol-Nadal, R.: Otsun, a python package for the optical analysis of solar-thermal collectors and photovoltaic cells with arbitrary geometry. Plos one **15**(10), 0240735 (2020)

[17] Branke, R., Heimsath, A.: Raytrace3d power tower-a novel optical model for central receiver systems. In: SolarPACES 2010, 16th Solar Power And Chemical Energy Systems International Symposium (2010)

[18] Hanrieder, N., Wilbert, S., Mancera-Guevara, D., Buck, R., Giuliano, S., Pitz-Paal, R.: Atmospheric extinction in solar tower plants–a review. Solar Energy **152**, 193–207 (2017)

[19] Guo, M., Sun, F., Wang, Z.: The backward ray tracing with effective solar brightness used to simulate the concentrated flux map of a solar tower concentrator. In: AIP Conference Proceedings, vol. 1850, p. 030023 (2017). AIP Publishing LLC

[20] Hastings, W.K.: Monte carlo sampling methods using markov chains and their applications (1970)

[21] Ahlrichs, P., Dünweg, B.: Lattice-boltzmann simulation of polymer-solvent systems. International Journal of Modern Physics C **9**(08), 1429–1438 (1998)

[22] Piegl, L., Tiller, W., Piegl, L., Tiller, W.: Rational b-spline curves and surfaces. The NURBS book, 117–139 (1995)

[23] Paszke, A., Gross, S., Massa, F., Lerer, A., Bradbury, J., Chanan, G., Killeen, T., Lin, Z., Gimelshein, N., Antiga, L., et al.: Pytorch: An imperative style, high-performance deep learning library. arxiv 2019. arXiv preprint arXiv:1912.01703 (1912)

[24] Zaibel, R., Dagan, E., Karni, J., Ries, H.: An astigmatic corrected target-aligned heliostat for high concentration. Solar Energy Materials and Solar Cells **37**(2), 191–202 (1995)

[25] Kajiya, J.T.: The rendering equation. In: Proceedings of the 13th Annual Conference on Computer Graphics and Interactive Techniques, pp. 143–150 (1986)

[26] Immel, D.S., Cohen, M.F., Greenberg, D.P.: A radiosity method for non-diffuse environments. Acm Siggraph Computer Graphics **20**(4), 133–142 (1986)

[27] Pargmann, M., Ebert, J., Kesselheim, S., Quinto, D.M., Pitz-Paal, R.: In situ enhancement of heliostat calibration using differentiable ray tracing and artificial intelligence. In: SolarPaces 2022 (2022). https://elib.dlr.de/189377/

[28] Pargmann, M., Ebert, J., Kesselheim, S., Quinto, D.M., Pitz-Paal, R.: Gradient-based power plant design using differentiable ray tracing. In: SolarPaces 2022 (2022). https://elib.dlr.de/189378/

[29] Prasad, A.D., Balu, A., Shah, H., Sarkar, S., Hegde, C., Krishnamurthy, A.: Nurbs-diff: A differentiable programming module for nurbs. Computer-Aided Design, 103199 (2022)

[30] de Boor, C.: A Practical Guide to Splines vol. 27, (1978). https://doi.org/10.2307/2006241